



Contraction-ratio variation and prediction of large experimental pressure-drops in sharp-corner circular contraction-expansions–Boger fluids



J.E. López-Aguilar^a, M.F. Webster^{a,*}, H.R. Tamaddon-Jahromi^a, M. Pérez-Camacho^b, O. Manero^c

^aInstitute of Non-Newtonian Fluid Mechanics, Swansea University, Bay Campus, College of Engineering, Fabian Way, Swansea, SA1 8EN, United Kingdom

^bFacultad de Estudios Superiores Zaragoza, Universidad Nacional Autónoma de México (UNAM), 09230, Mexico

^cInstituto de Investigaciones en Materiales, UNAM, 04510, Mexico

ARTICLE INFO

Article history:

Received 13 June 2016

Revised 13 September 2016

Accepted 20 October 2016

Available online 21 October 2016

Keywords:

epd-enhancement and flow-structure matching Boger-fluids, contraction-ratio variation
SwanINNFM model, numerical simulation
Lip, salient and elastic corner vortices
Continuum modelling

ABSTRACT

This study is concerned with the continuum modelling of sharp-corner contraction-expansion axisymmetric flows, under contraction-ratio variation, and more particularly, in the precise capture of the large-levels of experimental excess pressure-drops (*epd*) for Boger fluids. The particular contraction-ratios (α) considered are those studied experimentally by M. Pérez-Camacho, J.E. López-Aguilar, F. Calderas, O. Manero, M.F. Webster, J. Non-Newton. Fluid Mech. 222 (2015) 260–271; of $\alpha = \{2, 4, 6, 8, 10\}$. Their experimental PAA/corn-syrup Boger fluids have been characterized and modelled with the so-called swanINNFM model through dissipative continuum-scale modelling. This facilitates the precise capture of experimental-levels of *epd*-data (largest $epd = O(6)$ under $\alpha = 10$ contraction-ratio and sharp corners). The swanINNFM model has already proven capable of reproducing the large excess pressure-drops reported by J.P. Rothstein, G.H. McKinley, J. Non-Newton. Fluid Mech. 98 (2001) 33–63, in their experiments ($epd = O(3)$ for $\alpha = 4$ contraction-ratio and PS/PS Boger fluids); it is also capable of reproducing the Boger-fluid pressure-drop rise, relative to Newtonian-instance, in axisymmetric $\alpha = 4$ contraction-flow, as opposed to the null rise observed in the planar counterpart reported by S. Nigen, K. Walters, J. Non-Newton. Fluid Mech., 102 (2002) 343–359. In the present study, at each contraction-ratio and under *De*-rise (flow-rate-increase), one may identify two main phases: i) an *epd* plateauing-region at low deformation-rates, and ii) a sudden *epd*-rise above the Newtonian unity reference-line. With elevation in contraction-ratio, the first plateaued-*epd* phase is elongated and the maximum *epd*-levels rise significantly. Such *epd*-elevation is captured theoretically and numerically, with counterpart rise in extensional-viscosity. In addition, this position in *epd*-response correlates well against trends in vortex-dynamics - correctly capturing lip-vortex appearance, lip-vortex and salient-corner vortex co-existence and coalescence, and ultimate elastic corner-vortex domination. In this respect, their presence and transitions, may themselves be linked to increased elastic effects and normal-stress response.

© 2016 Elsevier B.V. All rights reserved.

1. Introduction

Experimentally, on entry-flow A plethora of steady-state studies have considered various: geometrical-configurations (axisymmetric-planar; contraction-ratio variation), edge-sharpness (sharp-rounded corners), and fluid rheology (constant shear-viscosity Boger fluids – shear-thinning fluids). For related background see [1–4]. Regarding *circular contractions and Boger fluids under a contraction-ratio of ($\alpha = 4$)*, Boger et al. [5] compared the

flow of two fluids with essentially equivalent characteristic relaxation times, derived from shear-flow measurement. Whilst increasing deformation-rate, observations revealed two distinct patterns arose in flow-structure. The first fluid, a polyacrylamide/corn-syrup solution (PAA/CS), displayed a single vortex, initially at low rates, confined to the salient-corner by a concave flow separation-line. This single vortex continually traversed from the corner to the lip with rate increase, bounded by a straightened separation-line and cell of constant reattachment-length. Then, once the vortex became located at the lip, it enhanced with further rise in flow-rate; attendant with growing reattachment-length and convex separation-line (cell-shape). A second test fluid, a polyisobuty-

* Corresponding author.

E-mail address: m.f.webster@swansea.ac.uk (M.F. Webster).

lene/polybutene solution (PIB/PB), exhibited isolated salient-corner and lip-vortices. Salient-corner vortex shrinkage and disappearance were reported, followed by lip-vortex formation and enhancement. These distinctly different forms of flow sequences were attributed to variation in extensional properties. The authors concluded that knowledge of steady and dynamic shear properties alone was insufficient to characterise elastic liquids in such complex flow scenarios. Subsequently, Boger and Binnington [6] studied the influence of aspect-ratio ($\alpha = \{4, 22\}$) for a well-known M1-fluid (a PIB/PB solution), concentrating upon circular geometries. Thereupon and with rising flow-rate, a similar pattern of isolated corner and lip-vortices was observed to that provided in Boger et al. [5], specifically for the relatively low aspect-ratio of $\alpha = 4$. Further incrementation in contraction-ratio to $\alpha = 22$, provided a rich sequence of structures, each displaying co-existence of salient-corner and lip-vortices. In this context and with rising flow-rate, this revealed patterns of: Newtonian flow-like structures at low deformation-rates; followed by corner and lip-vortex co-existence under an undulating flow separation-line; then, disappearance of the salient-corner vortex; and finally, lip-vortex domination. Such vortex-activity in this larger aspect-ratio, was attributed to the larger extension-rates generated therein. With a similar PIB/PB solution, McKinley et al. [7] also reported analogous trends under $\alpha = \{2, 3, 4, 5, 6, 8\}$. Once more, with co-existent of salient-corner and lip-vortices observed for $\alpha \geq 6$.

Excess pressure-drop in contraction-expansion geometries With focus on contraction-expansion flow, circular-symmetric and sharp-cornered, Rothstein and McKinley [8,9] provided results on excess pressure-drop (*epd*) and vortex dynamics for steady-state flow of a polystyrene-polystyrene (PS/PS)-based Boger fluid. There, with increase in Deborah number (*De*) (promoted via flow-rate *Q*-increase), Rothstein and McKinley [8] reported a marked rise in *epd* for ($\alpha = 4$) contraction-ratio. These authors remarked that such *epd*-rise was not related to an elastic-instability, instead attributing this to an additional polymeric dissipative-stress, observed when the material is stretched through a constriction. In subsequent work, Rothstein and McKinley [9] explored the influence of contraction-ratio and its variation for the same (PS/PS)-based Boger fluid, where both sharp- and rounded-corners were considered. Contraction-ratios of $\alpha = \{2, 4, 8\}$ provided large *epd* above their Newtonian counterparts, irrespective of the contraction-tip smoothness. Maximum *epd*-levels also rose with aspect-ratio increase. In terms of kinematic flow features, salient-corner dominated flow was prevalent for aspect-ratios of $\alpha \geq 4$, whilst lip-vortices were apparent for $\alpha = 2$. More recent experimental studies with a PAA/CS Boger fluid, of Perez-Camacho et al. [10] for $\alpha = \{2, 4, 6, 8, 10\}$, reported similar trends and findings, of increasing max-*epd* with contraction-ratio increase. In addition, transitions from salient-corner to lip-vortex domination were also recorded, yet only for relatively large contraction-ratios of $\alpha \geq 6$. Although such Boger-fluids are known to display similar shear rheometrical properties, their departure here in kinematic response is suspected to be linked to their respective extensional properties (hence formulation, see Rothstein and McKinley [9]).

Numerical predictions Traditionally, Boger fluids have been represented by constant shear-viscosity Oldroyd-B models. Nevertheless, Oldroyd-B solutions have failed to predict the significant increases observed experimentally in Couette correction (related to pressure drop) for Boger fluids (for example [11–16]). Moreover, the lack of finite-extensibility of the Oldroyd-B model, and its over-strong quadratic response in first normal stress difference N_1 , are severe shortcomings. These have been overcome more recently, via FENE-CR functionality [17]. Using the FENE-CR model, Szabo et al. [18] simulated a flow of Boger fluids through an axisymmetric ($\alpha = 4$) contraction-expansion with rounded-corners. This avoided numerical approximation difficulties associated with resolving the

flow about sharp-corners. These authors used a split Lagrangian-Eulerian finite-element scheme in their computations and extracted valuable information on *epd*. They used a solvent to total viscosity ratio (β) of 1/9 (benchmark highly-polymeric setting, far from Boger fluid composition), and varied the finite extensibility-parameter (*L*) of FENE-CR model. With values of $L = 3.26, 5$ and ∞ (Oldroyd-B limit), they gradually increased strain-hardening features, and hence, derived some modest *epd*-enhancement with *L*-increase (of $\sim 10\%$ at $De \sim 10$ with $L = 5$). More recently, Castillo-Tejas et al. [19] performed simulations for Boger fluids, through non-equilibrium molecular dynamics and on abrupt ($\alpha = \{2, 4\}$) contraction-expansion flows. Their molecular studies point the way forward, under planar and axisymmetric geometries, successfully predicting significant pressure-drop enhancement in the circular case (for $\alpha = 4$, of $\sim 150\%$ over the Newtonian unity reference-level; for $\alpha = 2$, of $\sim 40\%$, and null response for planar).

Contraction-flows, Boger and shear-thinning fluids: Aboubacar and Webster, [20] and Aboubacar et al. [11,21] switched attention to contraction geometries, again involving highly-polymeric solvent viscosity-ratio $\beta = 1/9$. Both planar and axisymmetric configurations were considered, with sharp versus rounded-corners. Using a hybrid finite element/volume method, numerical solutions for ($\alpha = 4$) aspect-ratio focussed on Couette-correction and vortex-dynamics, with Oldroyd-B and Phan-Thien-Tanner (PTT) models (Linear (LPTT) and Exponential (EPTT) variants [22]). There, on Couette-correction under $\varepsilon_{PTT} = 0.25$ for circular sharp-corner, LPTT initially dropped up to $Wi \sim 1$ and rose thereafter. In contrast, EPTT Couette-correction rose monotonically for all Wi , covering a wider elasticity range, whilst comparatively Oldroyd-B results dropped steeply to negative values over a narrow-restricted range of Wi . So, and conspicuously for Boger fluids, experimental-levels of pressure-drop were only poorly represented. It was argued that some of these trends were due to the relevant shifts and scaling that arise in the Couette-correction ratio, once shear-thinning is introduced. Under the same context of highly-polymeric $\beta = 1/9$ fluids, Oliveira et al. [23] focused on contraction-ratio variation in sharp-contractions ($\alpha \in [2, 100]$). Towards this end, a staggered-grid finite-volume method was used. Similarly, these authors provided results for Couette-correction and vortex-activity using Oldroyd-B (constant viscosity) and Phan-Thien-Tanner (LPTT) constitutive equations (*shear-thinning*). There, the vortex-type (corner, lip or mixed) was quantified in a 2D-map, with α and *De* as independent parameters. For $\alpha > 10$, lip-vortex formation occurred at a specific and fixed level of *De*. Moreover, at any constant value of *De*/ α , the salient-corner vortex completely surrounded that at the lip. In addition, parametric analysis was also conducted on the ε_{PTT} hardening-parameter, covering the range $\varepsilon_{PTT} = [0, 0.5]$. Couette-correction data somewhat replicated the trends reported in Aboubacar et al. [21]. For example, under $\varepsilon_{PTT} = 0.25$ and $10 \leq \alpha \leq 100$, Couette-correction was clustered around a single trend-line for all *De*. There, was an initial drop in Couette-correction, apparent up to $De \sim 1$, followed by a subsequent rise.

Nevertheless, and despite such advances in predictive capability described above, only recently have the remarkably large experimental *epd*-levels for the PS/PS-Boger fluid) of Rothstein and McKinley [9] been captured with continuum modelling ($\sim 300\%$ over the unity reference-line). This has been achieved with the so-called swanINNF model of Tamaddon-Jahromi et al. [24], within the relevant $\alpha = 4$ rounded-corner contraction-expansion flow of Rothstein and McKinley [9]. In addition, in the context of sharp-corner contraction entry-flow and using the same model, López-Aguilar et al. [25] have extended these ideas to apply to both planar and axisymmetric configurations. There and once again, the experimental pressure-drop data of Nigen and Walters [26] for PAA Boger-fluids, have been well reproduced, null response in planar and excessively large *epd* for circular. Such success relies on the swanIN-

NFM constitutive equation structure, which is a hybrid construct of a FENE-CR polymer component with a White-Metzner functional dependence of the extension-rate in both solvent and polymer contributions to the total stress. Hence, annunciation of the target for the present study, that is concerned with matching *epd*-levels reported in Perez-Camacho et al. [10], and the trace of counterpart vortex activity. Then, the geometry is that of contraction-expansion form, axisymmetric and sharp-cornered; the fluid is a Boger fluid of PAA/corn-syrup. The geometric ratios considered cover α -variation, $\alpha = \{2, 4, 6, 8, 10\}$. It is shown how *epd*-levels are closely extracted under swanINNFm modelling. With flow-rate rise and larger contraction-ratios, the vortex-dynamics reveals various flow transitions, from salient-corner to lip-dominated activity, replicating that reported in the counterpart experiments.

2. Governing equations and discretisation

The relevant governing equations are those of mass conservation and momentum transport, together with an equation of state for stress. Under isothermal and incompressible flow assumptions, these equations may be expressed as:

$$\nabla \cdot \mathbf{u} = 0, \tag{1}$$

$$Re \frac{\partial \mathbf{u}}{\partial t} = \nabla \cdot \mathbf{T} - Re \mathbf{u} \cdot \nabla \mathbf{u} - \nabla p, \tag{2}$$

where \mathbf{u} , represents fluid-velocity, p , isotropic pressure and \mathbf{T} , extra-stress. A first dimensionless group number, the Reynolds group-number $Re = (\rho \bar{U} R_c / \mu_o)$, provides a relative measure of inertial to viscous forces in the fluid. Here one identifies a material density as ρ , an average velocity based on the flow-rate Q as \bar{U} , a characteristic length of the flow domain as R_c (taken as the contraction-gap radius), and a characteristic viscosity as $\mu_o = \mu_p + \mu_s$. This characteristic viscosity is taken at zero shear-rate (simple-shear first-Newtonian viscosity-plateau), being split into two contributions, $\{\mu_p, \mu_s\}$ of {polymeric, solvent} origin. In this work, creeping flow is assumed, warranted through virtually inertialess [$Re \approx O(10^{-2})$] flow conditions.

Consistently then, the rheological nature of the fluid is specified through a solute-solvent split extra-stress \mathbf{T} , where $\mathbf{T} = \boldsymbol{\tau}_p + \boldsymbol{\tau}_s$; where $\boldsymbol{\tau}_p$ and $\boldsymbol{\tau}_s$ represent the polymeric (solute) and solvent stress-contributions, respectively. Under such splitting, a measure of the concentration of solute in the fluid-mixture, or solvent-fraction, may be defined as $\beta = \mu_s / \mu_o$. As required for Boger fluids, large solvent-fractions provide fluid-representation of solvent-dominated quality.

Constitutive equation – swanINNFm(q) model This model is a hybrid construct of a FENE-CR polymer component, with a White-Metzner functional dependence on extension-rate. It possesses both polymer and solvent dissipative terms (WM-FENE-CR; [17,24,25,27,28]). Such a model takes advantage of finite-extensibility, inherited from the parent FENE-CR model, with controlled-boosting of extensional-viscosity levels through a dissipative-stress contribution (WM-component). Moreover, a weakened N_{1Shear} response is obtained, in contrast to the strong quadratic response of Oldroyd-B.

In configuration-tensor \mathbf{A} -form, the swanINNFm(q) model may be expressed as:

$$\mathbf{T} = \boldsymbol{\tau}_p + \boldsymbol{\tau}_s = \frac{(1-\beta)}{De} f(Tr(|\mathbf{A}|)) \mathbf{A} \phi(\dot{\epsilon}) + 2\beta \phi(\dot{\epsilon}) \mathbf{D}, \tag{3}$$

$$De \overset{\nabla}{\mathbf{A}} + f(Tr(|\mathbf{A}|)) (\mathbf{A} - \mathbf{I}) = \mathbf{0}, \tag{4}$$

where $\overset{\nabla}{\mathbf{A}}$ represents the upper-convected material derivative of \mathbf{A} :

$$\overset{\nabla}{\mathbf{A}} = \frac{\partial \mathbf{A}}{\partial t} + \mathbf{u} \cdot \nabla \mathbf{A} - (\nabla \mathbf{u})^T \cdot \mathbf{A} - \mathbf{A} \cdot (\nabla \mathbf{u}). \tag{5}$$

$\mathbf{D} = (\nabla \mathbf{u} + \nabla \mathbf{u}^T) / 2$ is the rate-of-deformation tensor (superscript T for tensor transpose). Finally, the ABS- f -functional, $f(Tr(|\mathbf{A}|))$, in Eqs.(3) and (4) is taken as:

$$f(Tr(|\mathbf{A}|)) = \frac{1}{1 - Tr(|\mathbf{A}|)/L^2}, \tag{6}$$

where, the extensibility-parameter L governs the plateau-level of extensional viscosity η_{Ext} , and the slope strength of N_{1Shear} . Here, elevation in L -parameter results in larger η_{Ext} -plateaux and stronger N_{1Shear} -slopes, approaching the Oldroyd-B quadratic limit as $L \rightarrow \infty$.

A second non-dimensional group number, that of Deborah number $De = \lambda_1 \bar{U} / R_c$, may be defined through the ratio of a characteristic *time-of-the-material* λ_1 , and a characteristic *time-of-the-flow*. This flow characteristic-time is chosen as (R_c / \bar{U}) , and represents an average residence-time of a volume-element of fluid in the contraction-gap. As such, this non-dimensional De modulates the degree of viscoelasticity in the flow and correlates linearly with flow-rate (Q) -rise.

Within the White-Metzner construction, the dissipative-function $\phi(\dot{\epsilon})$ may be defined as $\phi(\dot{\epsilon}) = 1 + (\lambda_D \dot{\epsilon})^2$. This represents a quadratic-term truncated Taylor series approximation, of the more general hyperbolic-cosine function $\phi(\dot{\epsilon}) = \cosh(\lambda_D \dot{\epsilon})$ [24,29,30]. Here, λ_D represents a dissipative extensional-viscous time-scale (material dissipative-factor) and $\dot{\epsilon}$ an extension-rate.¹ The function $\phi(\dot{\epsilon})$ introduces additional dissipative-stress factors in both polymeric and solvent contributions to the stress tensor, see Eq. (3). These dissipative-stress contributions promote extra energy-removal from the flow [8]. Such loss of energy may be observed through large excess pressure-drop in contraction/contraction-expansion complex flows. The dissipative-factor λ_D is a time-parameter that governs the dissipative stress contribution, controlling the extensional viscosity boosting. The dissipative-factor λ_D may vary between $[0, \infty)$. Note that the swanINNFm(q) model collapses into FENE-CR [$\phi(\dot{\epsilon}) = 1$] in: ideal flows with null extensional deformation (via $\dot{\epsilon} = 0$; for example, pure shear and planar flows); or indeed, when the extra dissipative stress is deactivated through $\lambda_D = 0$.

Material function matching – First-normal stress difference N_{1Shear} The physical quantities reflecting the viscoelastic characteristics of the polyacrylamide (PAA)/corn-syrup(CS) Boger fluid are - a relaxation time of $\lambda_1^{Exp} = 0.174$ s and a zero-shear viscosity of $\eta_0^{Exp} = 13.5$ Pa s. In addition, N_{1Shear} data was provided in [10] (see Appendix A for scaling-factor equivalence on De numbers from experiments to simulation). In the range of shear-rate tested experimentally, the N_{1Shear} experimental data is well captured within the modelling through parameter selection of - a solvent fraction of $\beta = 0.9$ and an extensibility-parameter window of $L = \{3, 10\}$ (see [10]). Hence in the present study, a representative parameter set of $\{\beta, L\} = \{0.9, 5\}$ has been chosen.

The rheometric response of the swanINNFm(q) model is displayed in Fig. 1. The model predicts a constant shear viscosity, yet the first normal stress difference (N_{1Shear}) is weaker than the strong quadratic form exhibited by the Oldroyd-B model. The extensional data in Fig. 1a for the extensional viscosity (η_{Ext}) of the swanINNFm(q) model are new contributions specific to the viscoelastic setting for the range of $0 \leq \lambda_D \leq 1.0$. Here and for low extensional strain-rates up to 0.3, this model-response is practically identical to that of the Oldroyd-B model. Beyond this state, η_{Ext} for the $\lambda_D = 0$ (FENE-CR) model is capped, with η_{Ext} limiting-plateau levels depending on L -elevation. Here, one is able to detect the consequence of larger λ_D influence on η_{Ext} . For $\lambda_D > 0$, a rising trend in

¹ In complex flow, a generalized strain-rate $\dot{\epsilon}$ and a shear-rate $\dot{\gamma}$ may be extracted from the second and third invariants of rate-of-deformation tensor \mathbf{D} , viz, $\dot{\epsilon} = 3\mathbb{III}_D / \mathbb{II}_D$, and $\dot{\gamma} = 2\sqrt{\mathbb{II}_D}$; where $\mathbb{II}_D = \frac{1}{2} tr(\mathbf{D}^2)$, $\mathbb{III}_D = det(\mathbf{D})$.

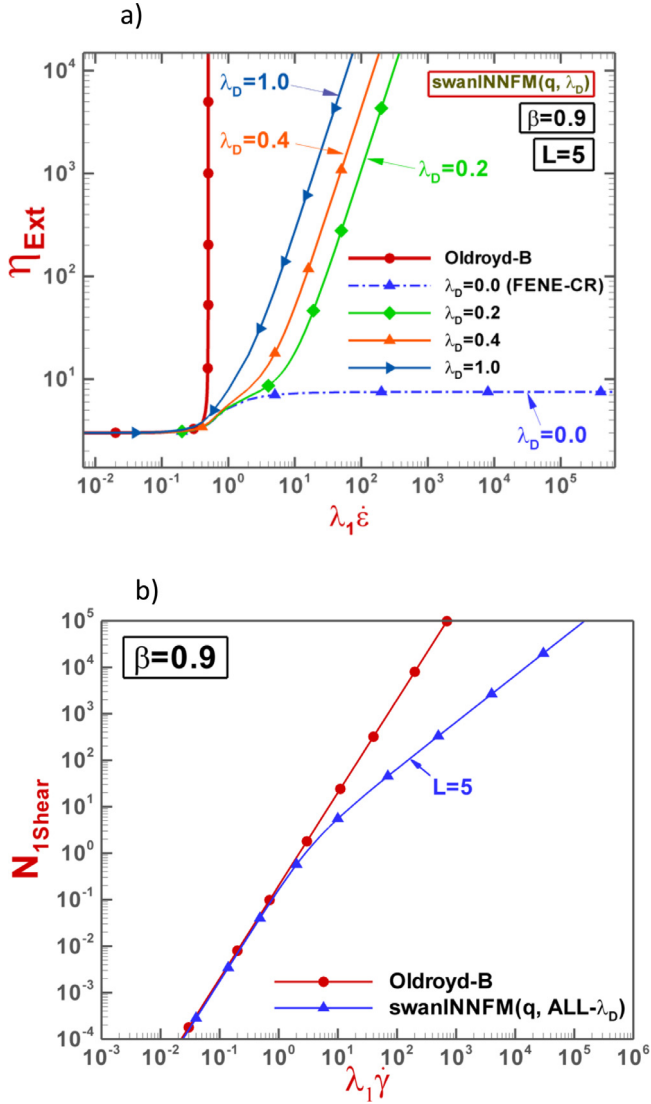


Fig. 1. Material functions; a) η_{Ext} & b) N_{1Shear} ; $\{\beta, L\} = \{0.9, 5\}$.

extensional viscosity is observed for swanINNFM(q), when compared to the FENE-CR base-model. Hence for example, with $\lambda_D=0.2$ and at strain-rates of $O(1)$ unit, extensional viscosity is around 5.5 units, whilst for $\lambda_D=1.0$, η_{Ext} has reached around ~ 8 units. With a five times increase in strain-rate [from $O(1)$ to $O(5)$], the corresponding η_{Ext} -levels are around $\{10, 80\}$ units for $\lambda_D=\{0.2, 1.0\}$, respectively. The relevant rheometrical functions for the swanINNFM(q) model are then:

$$\eta = \eta_0, \quad N_{1Shear} = \frac{2\eta_0(1-\beta)De\dot{\gamma}^2}{f}, \quad N_{2Shear} = 0,$$

$$\eta_{Ext} = 3\phi(\dot{\epsilon})\beta\eta_0 + 3\phi(\dot{\epsilon})(1-\beta)\eta_0 \left[\frac{f^2}{(f-2De\dot{\epsilon})(f+De\dot{\epsilon})} \right]. \quad (7)$$

Hence, it becomes clear that for a particular material, the $\phi(\dot{\epsilon})$ functional and its dissipative-factor λ_D , can be determined from fitting to extensional viscosity data; hence covering a range of deformation-rates, as experienced under alternative flow and geometric settings. Yet, when not available, we have been able to indicate through prediction in Nyström et al. [31], that fitting to experimental epd -measurement data can be used to back-calculate a measure for extensional viscosity. Specifically in Nyström et al. [31], considering an axisymmetric hyperbolic

contraction-expansion configuration in which a steady and constant strain-rate is established, it is shown that a parametric relationship between extensional viscosity (η_{Ext}) and pressure drop (epd) can be established. This has led to a practical means to find a best-fit to measured- epd from predicted- epd (simulation), and hence, to determine an extensional-based material time-constant λ_D . In this manner and for elastic fluids, a much-sought for measure of extensional viscosity can be established through the derived pressure-drop data.

Sharp-corner contraction-expansion flow domain & meshing The relevant mesh characteristic detail, covering the specific meshes employed within this study, is provided in Table 1. A schematic illustration is shown in Fig. 2, based on the $\alpha=8$ aspect-ratio geometry. Here, the aspect-ratio α denotes relative change in upstream-tube diameter to constriction diameter (held fixed at $R_c=1$ unit) for all contraction-ratios cited. Mesh-refinement analysis is conducted for the isolated benchmark-case of $\alpha=4$ contraction-ratio, drawing upon coarse, medium and refined meshes. As a consequence of findings therein, and with alternative aspect-ratios in mind, only medium refinement has been employed, accordingly. One notes that mesh-structure proved key in attaining highly-elastic solutions through the present Q -increase procedure. With focus on the constriction-zone at each aspect-ratio, meshes with uniform squared-structure construction (Fig. 2), provided solutions at significantly larger Q -levels (Wi_{crit}), than other options with trapezoidal mesh-structure (as constructed with areas delimited by diagonals uniting the centreline with the re-entrant corner contraction-tips). Such results are attributed to numerical stability gains from larger CFL numbers, due to a larger minimum-mesh size R_{min} for squared-structure meshes; these R_{min} -values are an order-of-magnitude larger than those for the trapezoidal-structured options.

Numerical approximation Comprehensive detail on the numerical fe/fv algorithm employed to generate the present predictive solutions can be found elsewhere [25]. Concisely, this scheme is that of a hybrid finite element/finite volume algorithm which follows a three-stage time-splitting semi-implicit formulation. Note, across contraction-ratios, singularities at re-entrant corners were not an impediment for matching epd -experimental data in the De -ranges sampled. New to this hybrid algorithmic formulation are techniques in strain-rate stabilisation (SRS-term - Belblidia et al. [32–34]); handling ABS- f -correction ($f(Tr(|\mathbf{A}|))$) in the constitutive equation, which provides consistent material-property prediction; and introducing purely-extensional velocity-gradient component specification at the shear-free centreline of the flow, through a velocity gradient (VGR) correction, López-Aguilar et al. [35]. At entry-exit zones, locally periodic boundary conditions were imposed, to overcome inconsistencies between inlet (and outlet) and inner-field approximations. Here, within the entry-zone a feedback procedure was implemented from the interior shear-flow section (likewise with an interior-domain feed-forward procedure for the exit-zone), notably active on velocity-gradients ($\nabla \mathbf{u}$) and extra-stress ($\boldsymbol{\tau}_p$), see López-Aguilar et al. [36]. The optimum solution continuation procedure adopted at each new flow rate is to first compute the best match extensional inelastic solution (swanINNFM($\lambda_D \neq 0, \lambda_1 = 0$)) to the experimental epd -level. Then, to use solution parameter continuation through the relaxation time (λ_1) to introduce elasticity, with swanINNFM($\lambda_D \neq 0, \lambda_1 \neq 0$).

3. On excess pressure-drops (epd)

Graphical plots for epd against flow-rate Q -increase (De -increase) are provided in Fig. 3. Here, one may recall that larger Q -levels, imply larger deformation-rates. This covers data for all five geometry aspect ratios considered, $\alpha=\{2, 4, 6, 8, 10\}$.

Table 1
Mesh characteristics.

Contraction Ratio α	Level of refinement	Number of elements	Total number of nodes	DOF	R_{\min}
2	Medium	3003	6204	38,825	0.0525
4	Coarse	1872	3905	24,447	0.1158
	Medium	2703	5600	35,049	0.0579
	Refined	4511	9274	58,026	0.0289
6	Medium	3056	6313	39,507	0.0582
8	Medium	2508	5217	32,657	0.0244
10	Medium	3112	6445	40,337	0.0241

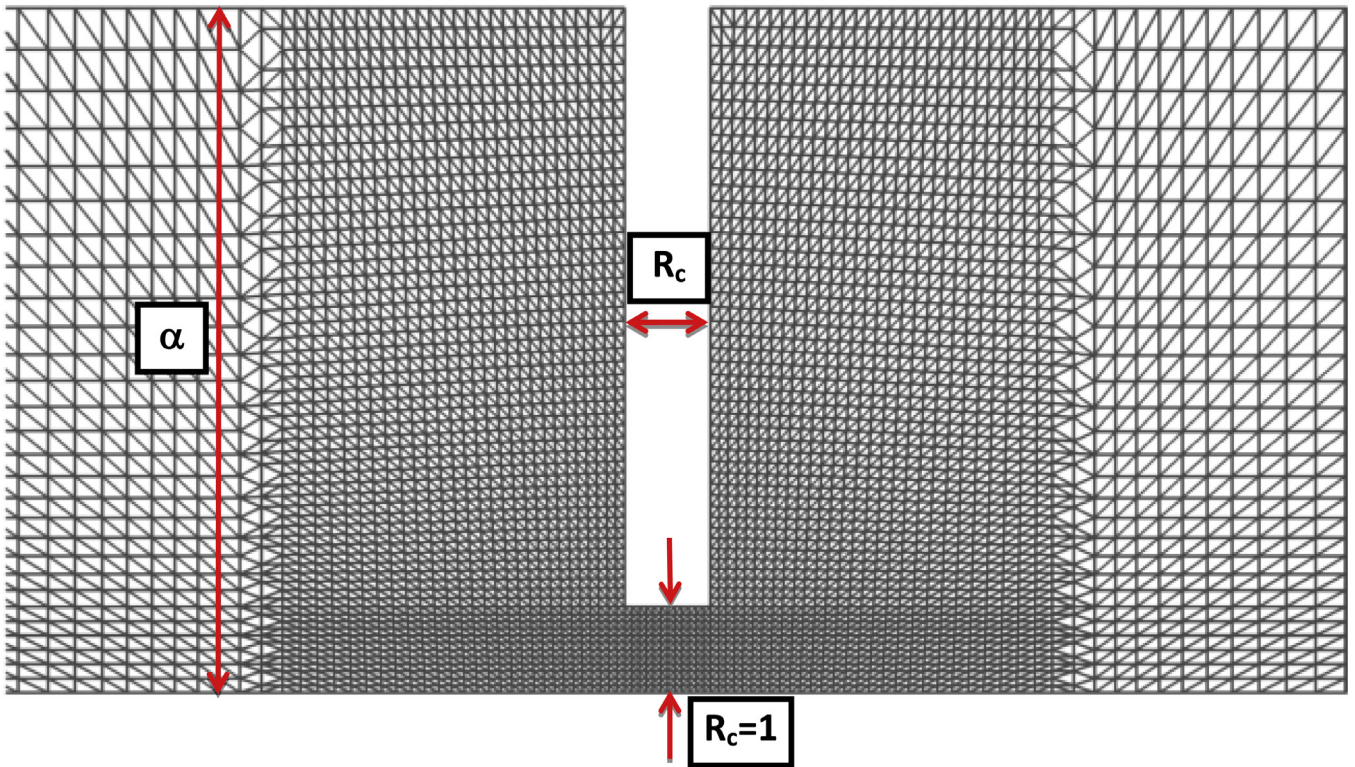


Fig. 2. Sharp contraction-expansion geometry mesh; $\alpha = \{2, 4, 6, 8, 10\}$; medium level of refinement.

$\alpha = 4$ contraction-ratio (base-case, Fig. 3b): When considering Q -rise, and whilst also applicable for all $\alpha \geq 4$, epd data display three main regions of epd -response. For $\alpha = 4$ the position is depicted as: (i) a first lower-rate epd -plateau zone, with $epd \sim 1$ ($De < 0.6$); (ii) a sharply rising - epd zone ($0.6 < De < 1.3$); and (iii) a tendency towards a second higher-rate epd -plateau ($De > 1.3$) (more clearly captured with larger aspect-ratio, of say $\alpha = 10$).

Pressure-drop ($\alpha = 4$)-maxima reach an order of $epd \sim 1.42$. Firstly, epd -data founded on predictions with the base-model FENE-CR (swanINNFM $\lambda_D = 0.0$, $L = 5$, $\beta = 0.9$) are provided (as shown in [10,24]). Conspicuously, in Fig. 3b, predictive-solution ($\lambda_D = 0.0$)-data lies significantly below experimental expectation in the higher deformation-rate region of $De > 0.6$. Here, it is shown how by appealing to the new swanINNFM ($\lambda_D \neq 0$) model, such under-prediction may be successfully overcome, so that the span of the experimental data may be well captured. Best practice would indicate that a Q -increase mode is the more practical and efficient steady-state solution-seeking route through continuation to implement such predictive matching [24]. That is, when taken against its alternative continuation-procedure of fluid-elasticity λ_1 -increase mode – a standard practice used under simulation procedures.

EpD λ_D -windows Employing fixed λ_D -solutions, the three main epd -($\alpha = 4$)-regions of response, identified above, are captured for

the De -range ($0 \leq De \leq 1.3$), in upper-lower windows of λ_D -values (see continuous lines in Fig. 3b). The first lower-window, is given by $\lambda_D = [0.0, 0.5]$, which covers the first lower-rate epd -plateau zone, just above epd -unity line, and slightly beyond up to $De \leq 0.8$. The second and upper-window, with $\lambda_D = [0.5, 0.8]$, captures the pronounced rising-trend observed in the experimental epd -data throughout the range $0.8 \leq De \leq 1.4$. One notes that for all $\alpha = 4$ -instances and for the lower plateaued- epd phases, the lower λ_D -bound is provided by $\lambda_D = 0$ solutions (FENE-CR limit; see Fig. 1 for back-reference to material functions). In this fashion, even the initial drop below the unity epd -reference-line is extracted (Fig. 3b,c for $\alpha = \{4, 6\}$).

EpD -data subsets Upon more close inspection of the epd -data in Fig. 3b, one may go somewhat further to classify three epd ranges, and accordingly three epd -data subsets. Here, it is the slope of the linear-fit line to each epd -data subset which is the distinguishing factor, as noted in De -ranges {I, II, III}. Crucially, this slope may be correlated against an averaged λ_D -value across each De -range identified. Such an average λ_D -value may be established by sampling λ_D -values that match the experimental epd -levels across a particular De -range. For example in the $\alpha = 4$ base-case, this suggests a step-function of λ_D -values, spanning such epd subsets/ De -ranges, identified through: (I) $\lambda_D = 0$, at relatively low flow-rates ($De \leq 0.65$); (II) $\lambda_D = 0.4$, at intermediate

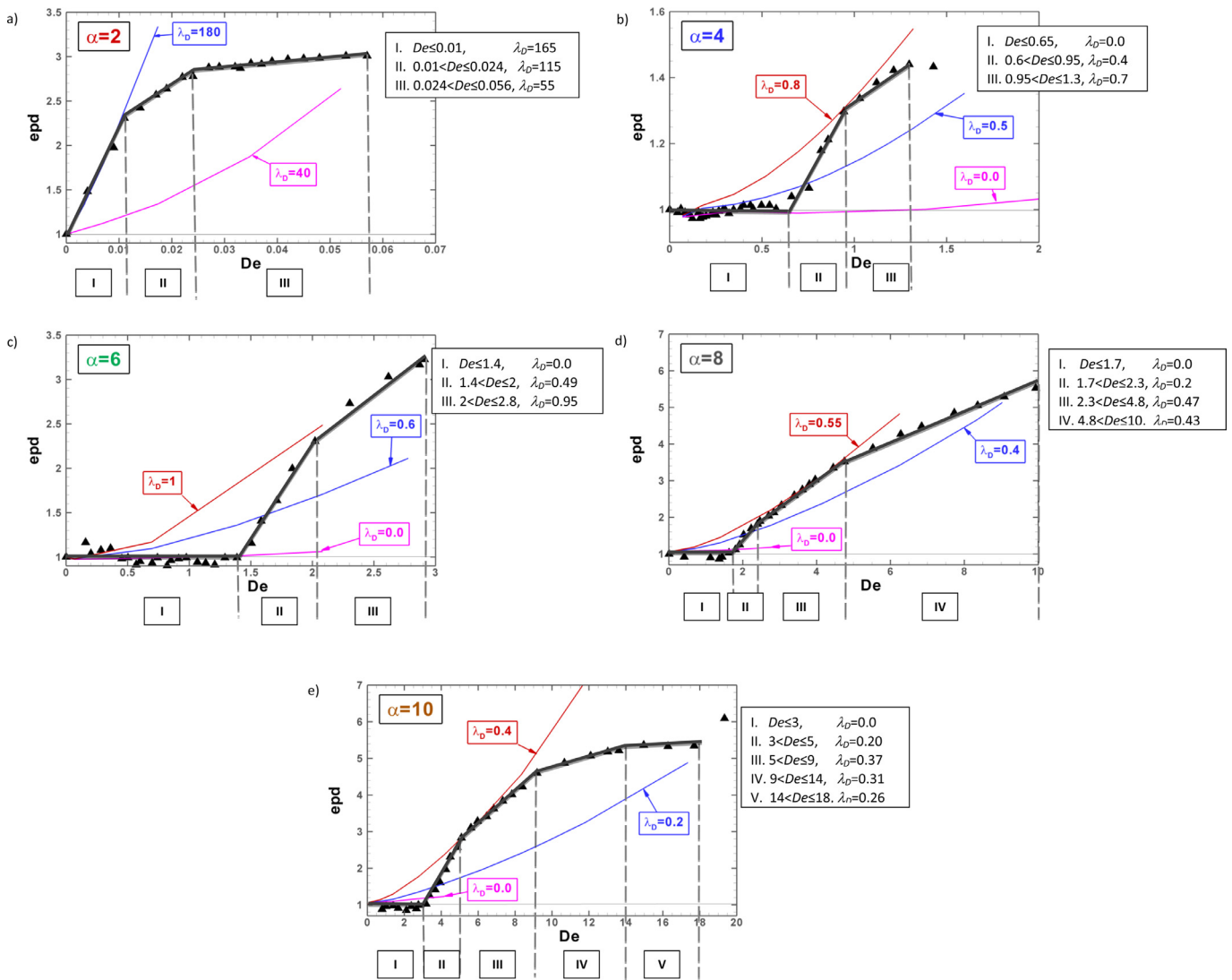


Fig. 3. epd prediction-windows against De ; {a, b, c, d, e} correspond to $\alpha = \{2, 4, 6, 8, 10\}$; experimental data-symbols, numerical predictions-lines.

flow-rates ($0.6 < De \leq 0.95$); and (III) $\lambda_D=0.7$, at high flow-rates ($0.95 < De \leq 1.3$).

$\alpha \geq 6$ contraction-ratio variation To progress across alternative deformation states, one may contrast epd -findings with larger geometric aspect-ratios, $\alpha \geq 6$. Note that with α -increase, firstly experimental- epd maxima rise; and secondly, larger Q -levels (larger deformation-rates) are required to precisely capture the distinct character and phases of lower epd -plateau, epd -rise and higher epd -plateau.

Matching epd -rise phase, aspect-ratio α -variation Seeking a match against the experimental data and with rise in α , it is clearly necessary to adjust the λ_D -parameter selection within the predictions. In contrast to the $\alpha=4$ base-case with a solution window of [lower, upper] bounds of $\lambda_D = [0.5, 0.8]$, the $\alpha=6$ case demands larger dissipative-parameter λ_D -levels (Fig. 3c). Hence, observing a fresh window and bounds of $\lambda_D = [0.6, 1.0]$. For yet larger contraction-ratios of $\alpha=8$, there is a sustained decrease in λ_D -levels to match the experimental epd (Fig. 3d,e). For example, in the $\alpha=8$ case, corresponding bounds are given under solution window $\lambda_D = [0.4, 0.55]$, whilst the $\alpha=10$ case requires a bounded-window of $\lambda_D = [0.2, 0.4]$. Such λ_D -reduction for $\alpha \geq 8$ may be correlated against ever increasing maximum extension-rates with α -rise. These larger extension-rates with α -rise are

promoted by the relatively larger Q -levels needed to substantiate the epd -rises detected in the experiments. This is a natural state of affairs, since the dissipative-function, $\phi(\lambda_D \dot{\epsilon}) = 1 + (\lambda_D \dot{\epsilon})^2$, itself has dependency upon the product factor $(\lambda_D \dot{\epsilon})$ as its driving parameter. Hence, for the same level of ϕ (whose increase stimulates larger η_E and epd), a larger extension-rate $\dot{\epsilon}$ automatically provides a smaller dissipative-parameter λ_D . Under such complex flow deformation, as here, this is strong evidence of the need for rate-dependent adjustment of the extensional-based dissipative parameter (λ_D) – as suggested by the step-function above, or indeed by a multimode representation (motivated by extensional considerations). In principal, upon using a more robust multimode approach, even better predictions against experimental findings may be anticipated, offering wider matching to experimental data in shear (η_{Shear}, N_{IShear}) than afforded by a single-mode averaged approximation.

To investigate such dependencies and interrogate the position further, plots are provided in Fig. 4 for centreline extension-rate maximum, $\dot{\epsilon}_{max}$, dissipative-factor λ_D and dissipative-function ϕ_{max} . Such data is taken against deformation-rate rise and across the various contraction-ratios. Note, these extrema are extracted at various Q -levels, each Q -level being representative of an epd -subset in each α -instance, from Fig. 3 data. The λ_D -values are those required

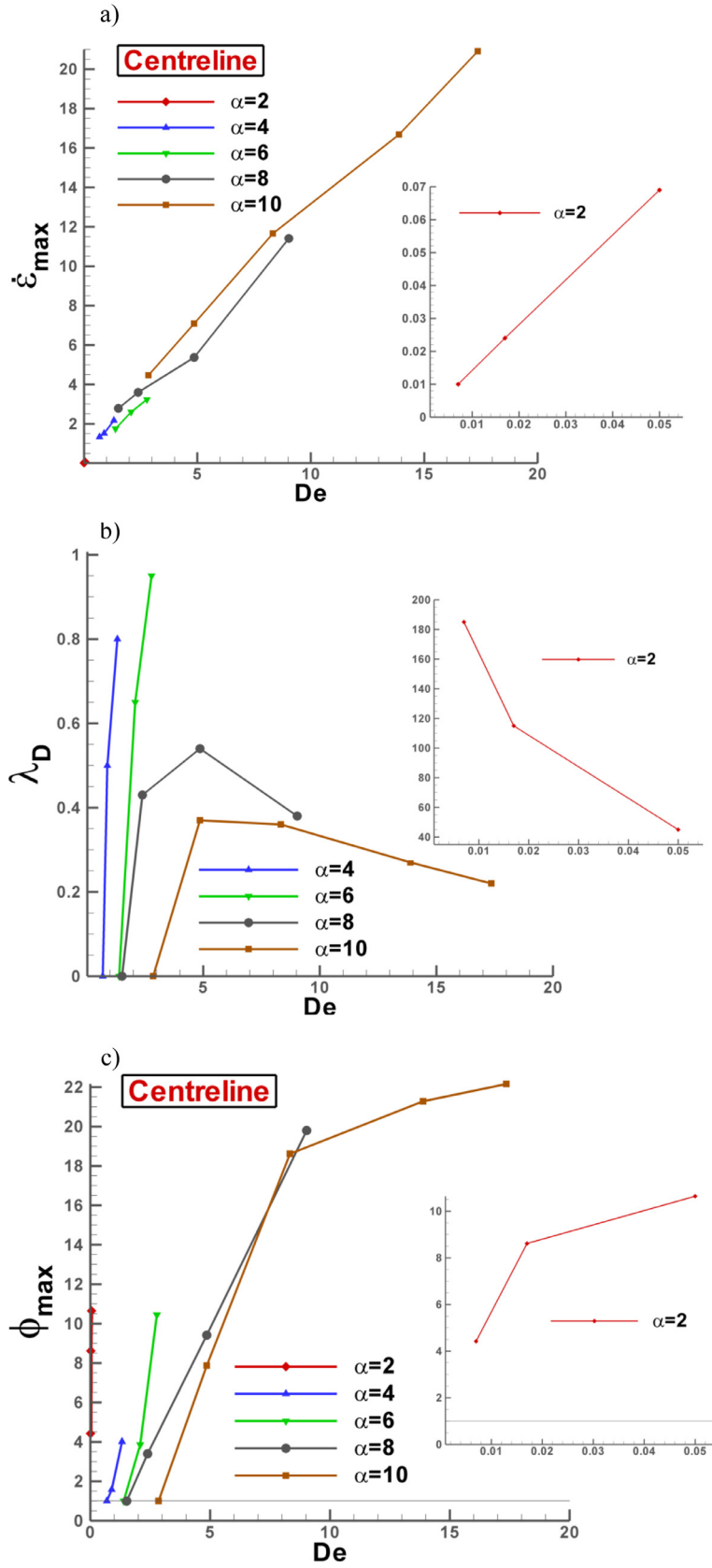


Fig. 4. Centreline a) $\dot{\epsilon}_{max}$, b) λ_D and c) ϕ_{max} against De ; $\alpha = \{2, 4, 6, 8, 10\}$.

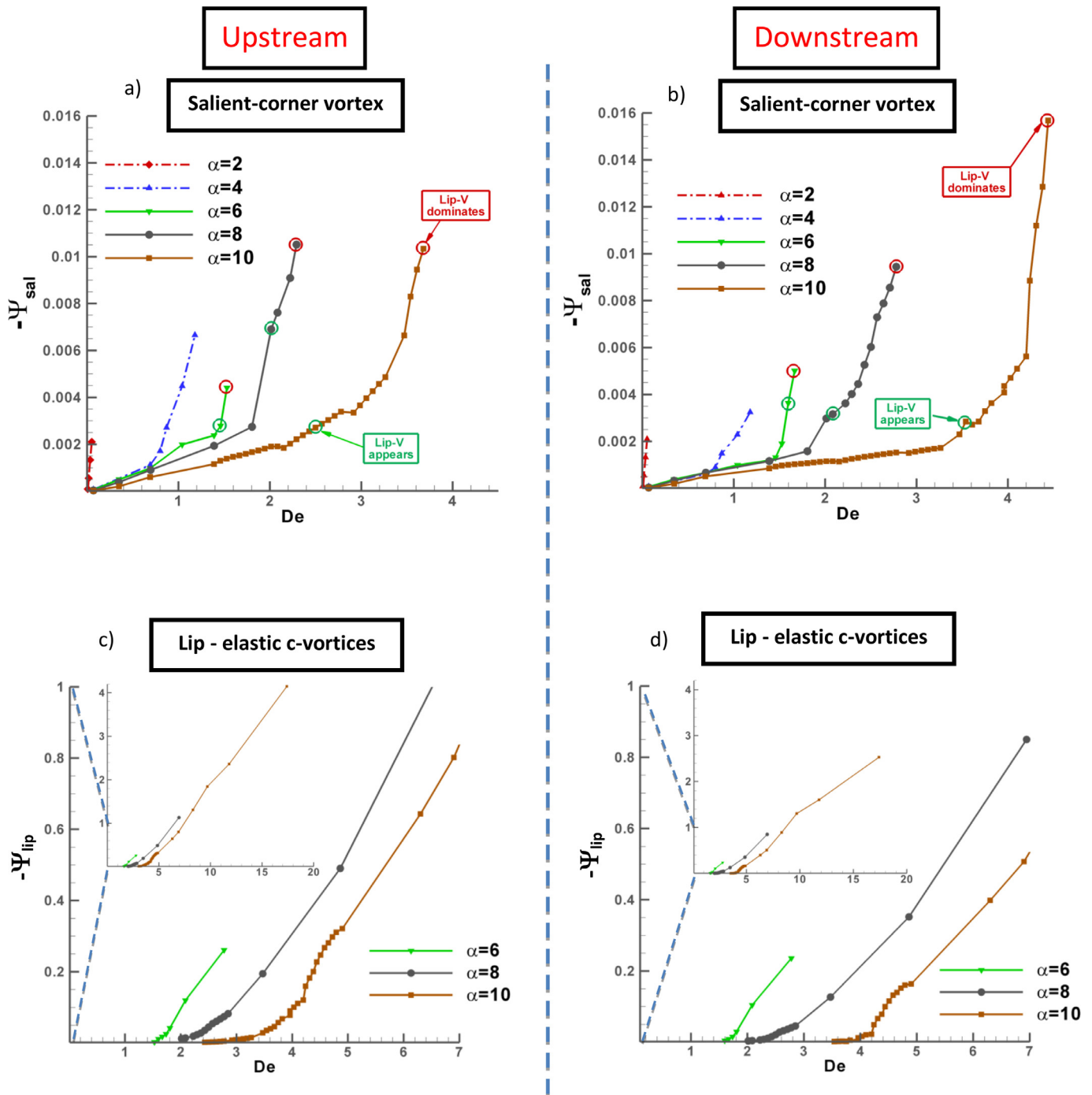


Fig. 5. Vortex intensity against De ; $\alpha = \{2, 4, 6, 8, 10\}$. (For interpretation of the references to colour in the text, the reader is referred to the web version of this article.)

to best match the experimental epd -data, in each α -instance, and at specific De -values (Q -levels). In Fig. 4a, with each α -instance, a linear relationship is recorded between the maximum extension-rate at the centreline $\dot{\epsilon}_{max}$ through De (Q -rise). At fixed- De (Q -fixed) and with α -rise, centreline $\dot{\epsilon}_{max}$ increases. For instance at $De=9$, $\alpha=8$ maximum extension-rate equates to $\dot{\epsilon}_{max}=11.5$ units, whilst equivalently for $\alpha=10$, $\dot{\epsilon}_{max}=12$ units; rendering a 4% increment. In contrast in Fig. 4b, covering the various α -instances, a complex non-linear dependency is observed to hold between λ_D with Q -rise. For example, with $\alpha=\{4, 6\}$ and Q -rise, steep linear increasing trends are apparent on λ_D ; whilst, for $\alpha=\{8, 10\}$, an initial (shallower) linear rise is observed at relatively small deformation-rates, followed by a maximum being reached, before

a subsequent decline. The consequence is gathered in the rising ϕ_{max} -trends as observed in Fig. 4c, which are relatively linear for $\alpha=\{4, 6, 8\}$, and piecewise-linear for $\alpha=10$.

EpD -data subsets and λ_D -step-functions ($\alpha \geq 6$) Taken in contrast to the $\alpha=4$ base-case, $\alpha \geq 8$ instances display richer behaviour in epd -slope subsets (Fig. 3c–e). Note, both $\alpha=4$ and $\alpha=6$ cases displays three long subsets, as observed in Fig. 3b,c. Generally and with α -rise, an increased number of subsets are required to match the experimental data, albeit for an ever widening coverage and De -range. In the extreme case of $\alpha=10$ (Fig. 3e), five subsets are identified: (I) $\lambda_D=0$ for $De \leq 3$; (II) $\lambda_D=0.2$ for $4 < De \leq 5$; (III) $\lambda_D=0.37$ for $5 < De \leq 9$; (IV) $\lambda_D=0.31$ for $9 < De \leq 14$; and (V) $\lambda_D=0.26$ for $14 < De \leq 18$). Meanwhile, the $\alpha=8$ instance

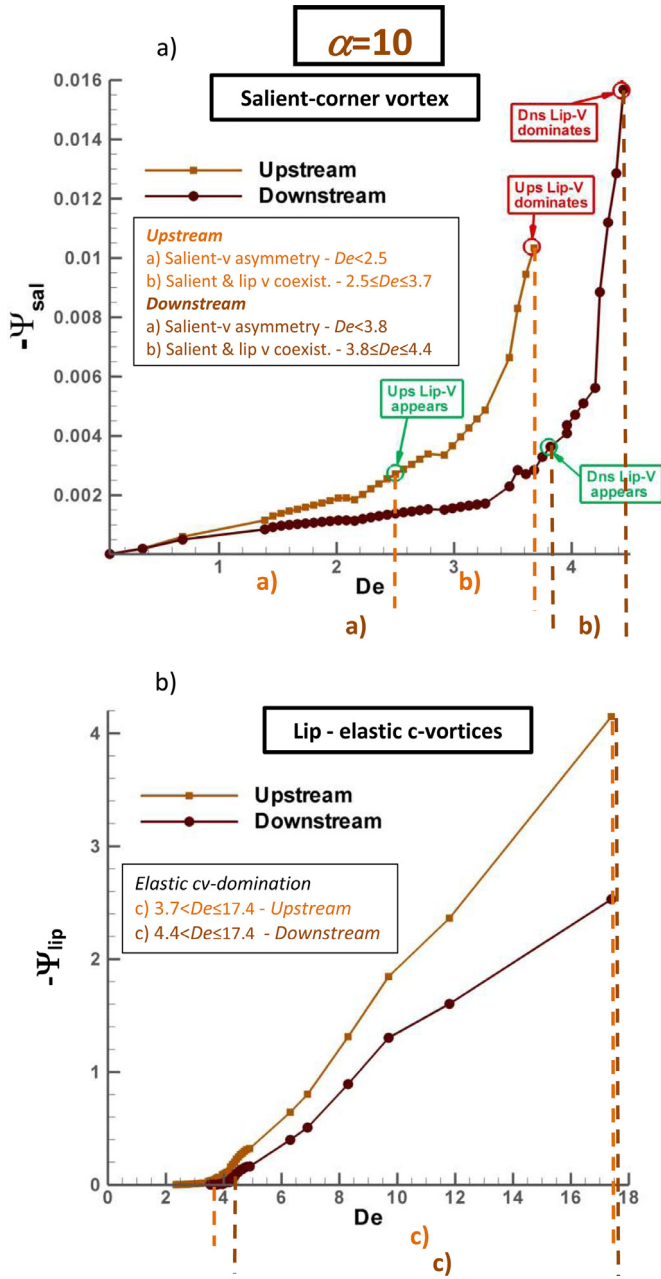


Fig. 6. Vortex intensity against De ; $\alpha = 10$.

displays four subsets (Fig. 3d): (I) $\lambda_D = 0$ for $De \leq 1.7$; (II) $\lambda_D = 0.2$ for $1.7 < De \leq 2.3$; (III) $\lambda_D = 0.47$ for $2.3 < De \leq 4.8$; and (IV) $\lambda_D = 0.43$ for $4.8 < De \leq 10$.

$\alpha = 2$ contraction-ratio variation This geometry choice is unique amongst its counterparts, in that it offers much reduced levels of maximum strain-rates (see Fig. 4a). This implies that larger levels of dissipative-factor λ_D [$=O(10^2)$, from the smallest Q -level] are required to furnish equivalent levels in the dissipation-function $\phi(\lambda_D \dot{\epsilon})$ (Fig. 4b,c), and hence impact upon the rheometrical functions. Notably, $\alpha = 2$ *epd*-data is devoid of the first lower *epd*-plateau, displaying only an initial sharp rise in *epd* from the *epd*-unity reference line. Then, at $De \sim 0.01$, a continuous slope-decrease is observed, to finally attain a constant yet rather shallow rising-trend for $De > 0.03$. Moreover, the *epd*-maximum level observed is $epd \sim 3$, which is twice that for the base-case of $\alpha = 4$ ($epd \sim 1.42$). Here, only a single window of λ_D -values is required to match *epd*-experimental data (Fig. 3a). The {lower, upper} bounds

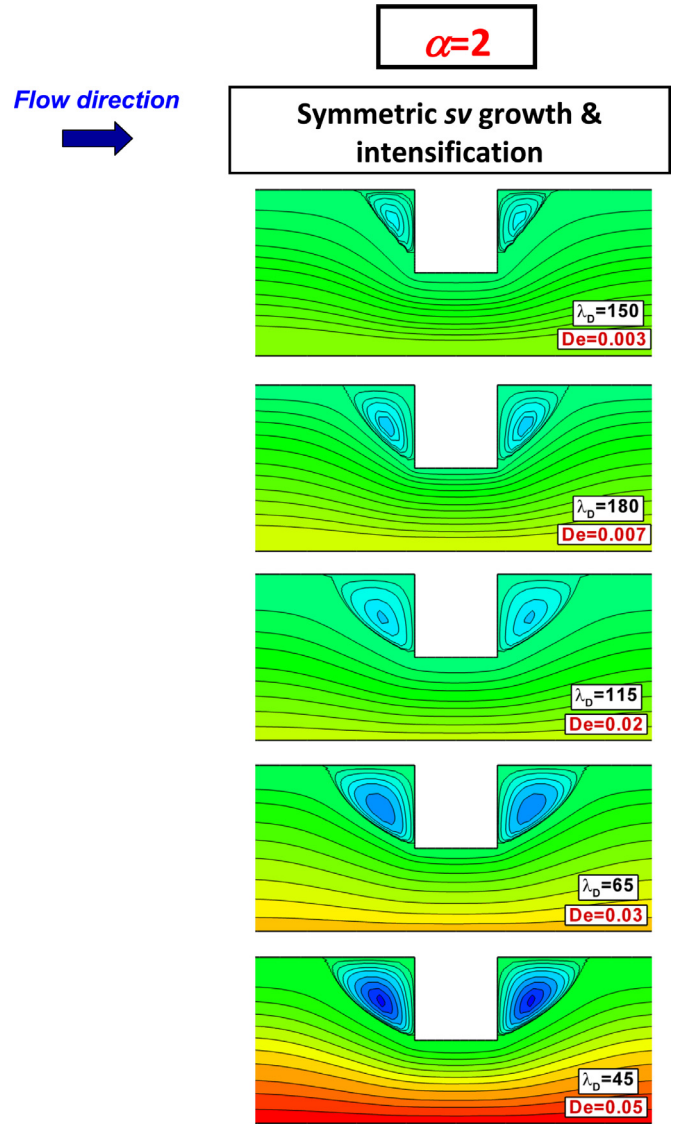


Fig. 7. Streamlines against De ; $\alpha = 2$.

of such a solution-window are given by $\lambda_D = [45, 180]$. Nevertheless, three *epd*-slope subsets remain to be identified: (I) $\lambda_D = 165$ for $De \leq 0.01$; (II) $\lambda_D = 115$ for $0.01 < De \leq 0.024$; and (III) $\lambda_D = 55$ for $0.024 < De \leq 0.056$. In contrast to larger- α and with Q -rise, the λ_D -level decreases whilst transcending these *epd*-subsets.

4. On vortex dynamics

In this section, particular consideration is given to flow structure, through vortex-intensity and streamlines patterns. Once again, this covers solution-data for all five geometry aspect-ratios, $\alpha = \{2, 4, 6, 8, 10\}$. In summary, with Q -rise (De -increase), a number of vortex features may be observed, upstream and downstream of the contraction. First, there is onset and rise in salient-corner (sv)-vortex-intensity, Ψ_{sal} (Figs. 5a,b and 6a), with concave-shape (Figs. 8, 9a–11a; $\alpha = 4$: upstream-downstream sv asymmetry and growth). Second, there is lip-vortex (*lv*)-formation in some cases, notably for $\alpha \geq 6$ cases (Figs. 9–11b). Third in these instances, the convex lip-vortex eventually dominates and evolves into an elastic corner-vortex (cv), but only at relatively large flow-rates (Ψ_{lip} : Figs. 5c,d and 6b; streamlines: Figs. 9–11c). One notes the use of absolute value notation for clarity on Ψ_{sal} and Ψ_{lip} . Such features have

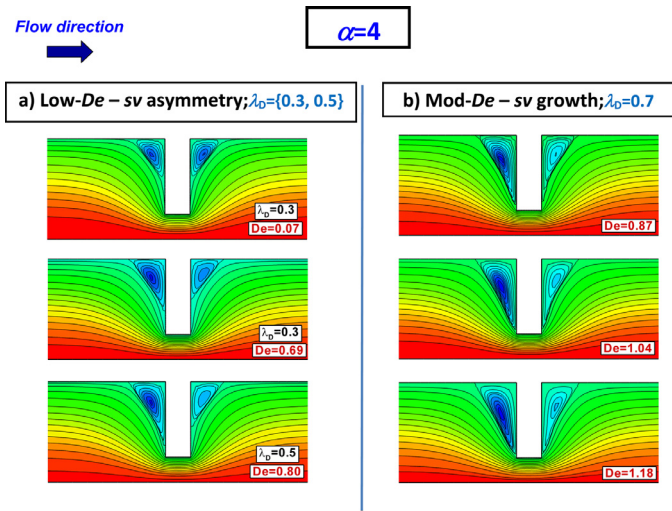


Fig. 8. Streamlines against De ; $\alpha = 4$.

their counterpart streamline-representation in Figs. 7–11. Such a sequence of vortex-growth patterns has been observed previously, under circular $\alpha = 4$ entry-flow experiments for a PIB/PB Boger-fluid flow (Boger et al. 1986). There, salient-corner and lip-vortices co-existed at mid- Q -levels; subsequently, the lip-vortex began to dominate and to ultimately develop into an elastic corner-vortex. Conspicuously, within an intermediate- Q range [$\alpha = \{4, 6, 8, 10\}$, $De \sim \{0.8, 1.5, 2, 3.5\}$], the appearance of a lip-vortex and its subsequent domination, coincides with epd -rise and departure from the unity reference-line. Such correspondence marks flow regime change, and this is well captured under $\lambda_D \neq 0$ solutions.

Comparison of vortex-intensity with α -variation In Fig. 5, trend plots of the salient-corner and lip-based vortex-activity are provided, for both upstream and downstream zones.

Ψ_{sal} -maxima, relative strength with α -variation In the $\alpha = 2$ case, despite its relatively low deformation-rates ($0.007 \leq De \leq 0.05$), a sharp rise in Ψ_{sal} is observed (Fig. 5a,b red-dashed lines), with a unique range of vortex-enhancement (symmetric convex vortices; see on to Fig. 7). Note, in Fig. 5a upstream, there is Ψ_{sal} -maxima rise from $\alpha = 2$ to 4; then decline from $\alpha = 4$ to 6; and finally rise for $\alpha \geq 6$. The initial appearance of a lip-vortex is also highlighted, alongside Ψ_{sal} -growth. Comparatively, Fig. 5b downstream, Ψ_{sal} -maxima enlarge with α -rise. Note that, with respect to the upstream-location, downstream Ψ_{sal} -maxima are always smaller, and for $\alpha \geq 6$, appear somewhat more delayed till larger Q -levels.

In Fig. 5c,d, counterpart lip vortex-intensity Ψ_{lip} -plots are provided (no lip-vortices present for $\alpha \leq 4$). With α -rise, lip-vortex onset is gradually shifted to larger Q -levels. Upstream, the first flow-rates to witness lip-vortex formation are $De = \{1.53, 2.01, 2.36\}$ for $\alpha = \{6, 8, 10\}$. From such positions, relatively sharp rise is observed in Ψ_{lip} . Then, at sufficiently high Q -levels, a linear Ψ_{lip} -trend is recovered (Fig. 5c,d), during a phase dominated by an elastic corner-vortex (see Figs. 9c,10,11c). Notably for $\alpha = \{6, 8, 10\}$ and on transition activity from salient-corner to elastic corner-vortex domination, predictions located at $De \sim \{2, 4, 7\}$, roughly coincide with experimental observations, reported at $De \sim \{2.6, 4.5, 7\}$ (see [10]).

$\alpha = 10$ instance Since the $\alpha = 10$ geometry provides the most prominent features (see streamline patterns, Figs. 7–11), this instance is isolated in Fig. 6, to display direct upstream-downstream data comparison (also representative for all $\alpha \geq 6$). For $\alpha = 10$, the upstream lip-vortex first appears at $De = 2.5$ (Fig. 6a). Before this stage ($De < 2.5$), there is salient-corner vortex asymmetry upstream-downstream (see counterpart Fig. 11a). Beyond $De > 2.5$,

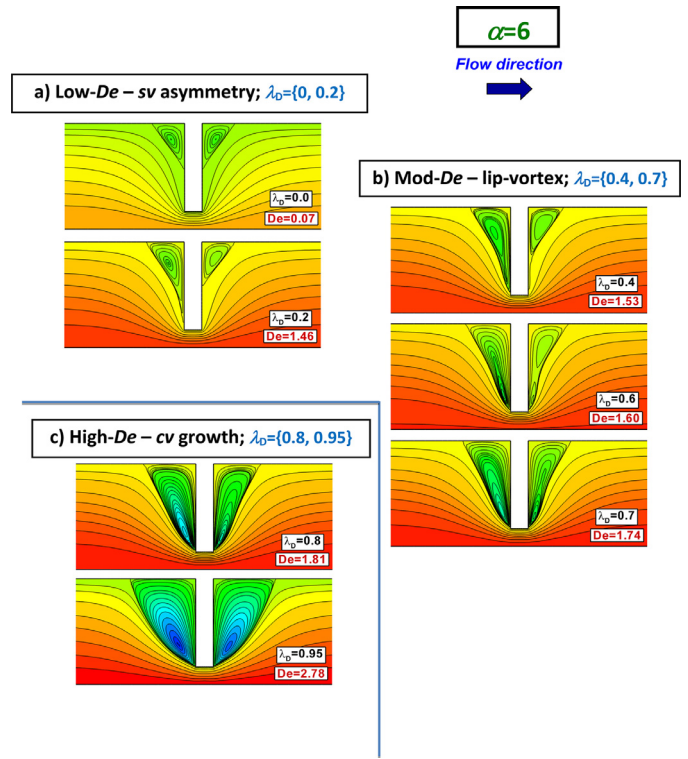


Fig. 9. Streamlines against De ; $\alpha = 6$.

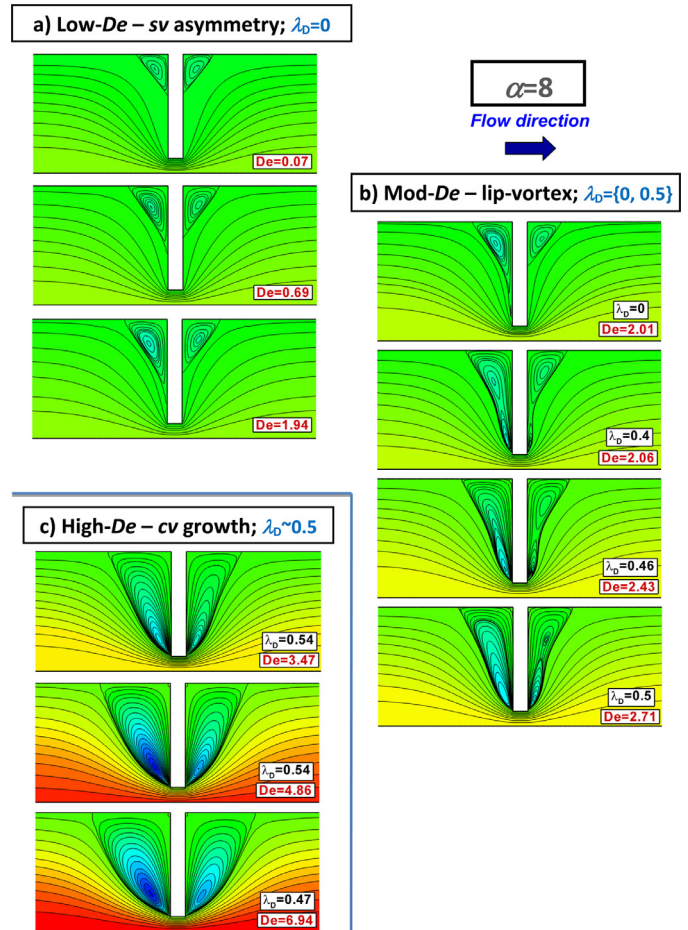


Fig. 10. Streamlines against De ; $\alpha = 8$.

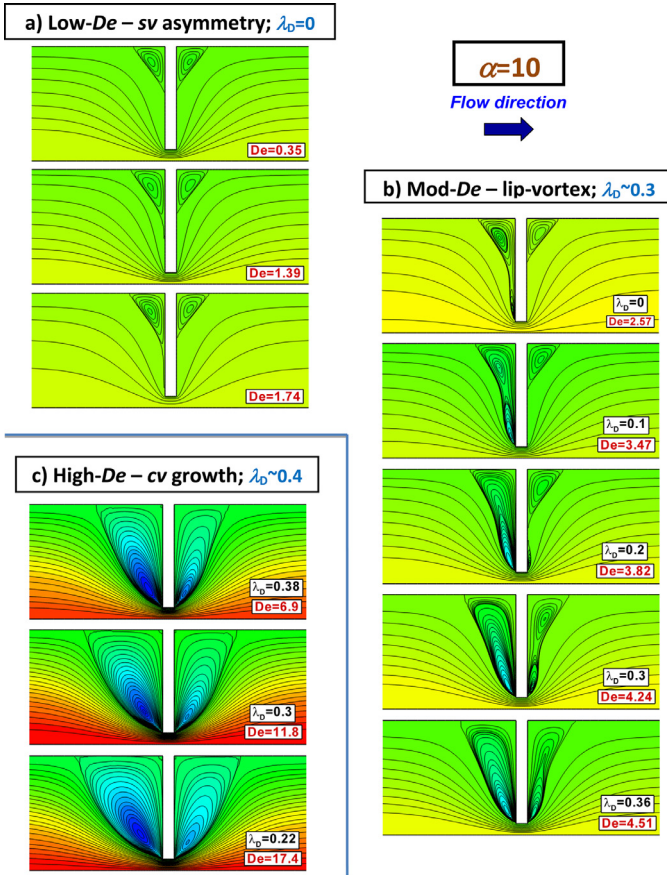


Fig. 11. Streamlines against De ; $\alpha = 10$.

the salient corner-vortex experiences a sharp rise in its rotational strength, before its disappearance at $De > 3.7$ [elastic corner-vortex domination identified, $4.5 < De \leq 17.4$ (Figs. 6b and 11c)]. There is co-existence of a salient-corner and lip-vortex for $2.5 \leq De \leq 4.5$ (Fig. 11b). Here, an increase of 260% in vortex intensity is observed via $\{\Psi_{sal}, De\}$, from $\{0.003, 2.57\}$ to $\{0.010, 3.68\}$. Note, there are similar trend patterns observed downstream, although these are somewhat delayed in deformation-rate; with lip-vortex appearance at $De = 3.8$, and elastic corner-vortex domination for $De > 4.4$.

Such De -ranges are affected by aspect ratio reduction from $\alpha = 10$ to $\alpha = \{6, 8\}$, becoming narrower in width and lower in starting value. For $\alpha = 6$ (Fig. 9) - (a) salient-corner vortex asymmetry: $De < 1.5$; (b) lip-vortex appearance: $De = 1.5$; and vortex co-existence: $1.5 \leq De \leq 1.7$; and (elastic corner-vortex domination: $1.7 < De \leq 2.8$. For $\alpha = 8$ (Fig. 10) - (a) salient-corner vortex asymmetry: $De < 2$, (b) lip-vortex appearance: $De = 2$; and vortex co-existence: $2.0 \leq De \leq 2.8$, and (c) elastic corner-vortex domination: $2.8 < De \leq 9$. One notes the elongation of the salient corner-vortex (concavity), observed at relatively low Q -levels (part a) of Figs. 9–11, is a key factor governing lip-vortex formation. Such elongation and further lip-vortex growth are enhanced by the relatively longer front and back wall-faces of the $\alpha = 10$ geometry. Hence, as α -increases, the strength and size of these emerging lip-vortices increase.

5. On stress-to-vortex structure interdependence

First normal stress ratio As proposed by Rothstein and McKinley [9], in their experimental study on aspect-ratio variation, there a normal stress-ratio was used to depict the transition from lip-vortex activity to elastic corner-vortex activity. Data on a variety

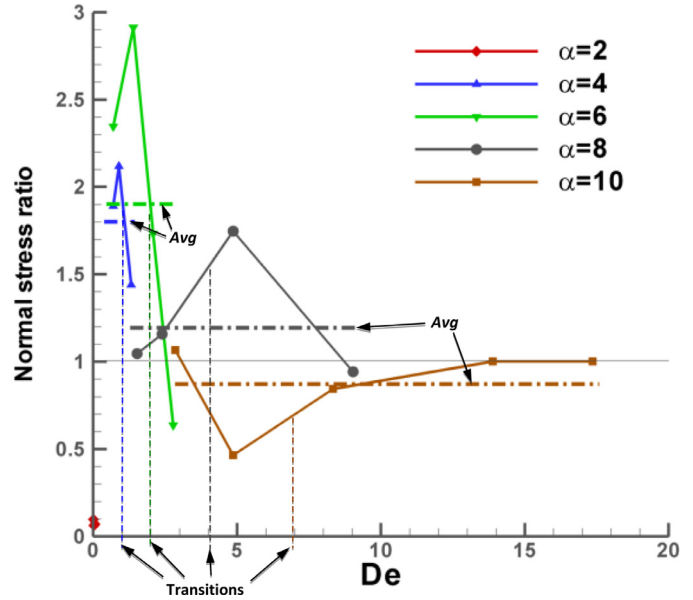


Fig. 12. Normal stress ratio against De ; $\alpha = \{2, 4, 6, 8, 10\}$.

of fluids was provided, and each at a specified but different flow-rate. Such a normal stress-ratio was defined as the relative measure of normal-stress in pure shear (as on walls), to that in pure extension (as on flow centreline). For large- α , these authors reported on phases of elastic corner-vortex domination, which correlated with relatively small normal stress-ratios; hence, with domination of extensional over shear normal-stress. Accordingly, Fig. 12 conveys representative and current findings on this normal stress-ratio. Here and for each α -instance in turn, treated in contrast to the Rothstein and McKinley data [9], normal stress-ratios are reported at various deformation-rates, as flow-rate is increased. With α -rise, our averaged normal stress-ratio (taken across flow-rate and indicated with a dash-dotted line), rises from ~ 1.8 units for $\alpha = 4$, to ~ 1.9 units for $\alpha = 6$. For larger aspect-ratios, these averaged-values subsequently decline sharply, to $\sim \{1.2, 0.9\}$ for $\{8, 10\}$. In line with findings of Rothstein and McKinley [9] through α -rise, such a decline in normal stress-ratio would indicate larger extensional- N_1 relative to that in shear. This position reflects elastic corner-vortex domination for $\alpha \geq 6$ at relatively high deformation-rates. Moreover, extrema are observed in normal stress-ratio for all $\alpha \geq 4$; occurring at $De \sim \{0.8, 1.1, 4.8, 5\}$ with $\alpha = \{4, 6, 8, 10\}$. Hence and consistently $\alpha \geq 6$ aspect-ratio solutions produce more balanced shear-extension normal-stress-ratios, revealing dominant elastic corner-vortex activity; whilst counterpart $\alpha = 4$ -solutions with larger normal-stress-ratios, provide exclusively salient-corner vortex-activity. Phase transitions, from lip-vortex to elastic corner-vortex are also indicated in Fig. 12 (by vertical dashed-lines), and arise in the vicinity of extrema in normal stress-ratio.

Vortex activity against normal stress differences, N_1 and N_2 Representative N_1 and N_2 field projections (3D) are compared in Fig. 13 against corresponding vortex transitions. Here, the most responsive case of aspect-ratio $\alpha = 10$ is selected, covering Q -rise through low-medium-high De of $0.35 \leq De \leq 17.4$. As such, vortex activity may be directly correlated to the corner-patterns apparent in N_1 - N_2 fields, observed through corner-to-lip vortices (structure and location, both upstream and downstream). One may infer from this evidence that elasticity, through N_1 - N_2 , is responsible for the formation and evolution of these corner and lip-vortices. At relatively low $De = 0.35$ (Fig. 13a), symmetric upstream-downstream normal-stress patterns are apparent, reflecting the presence of salient-corner vortex-like structures. During the vortex co-existence

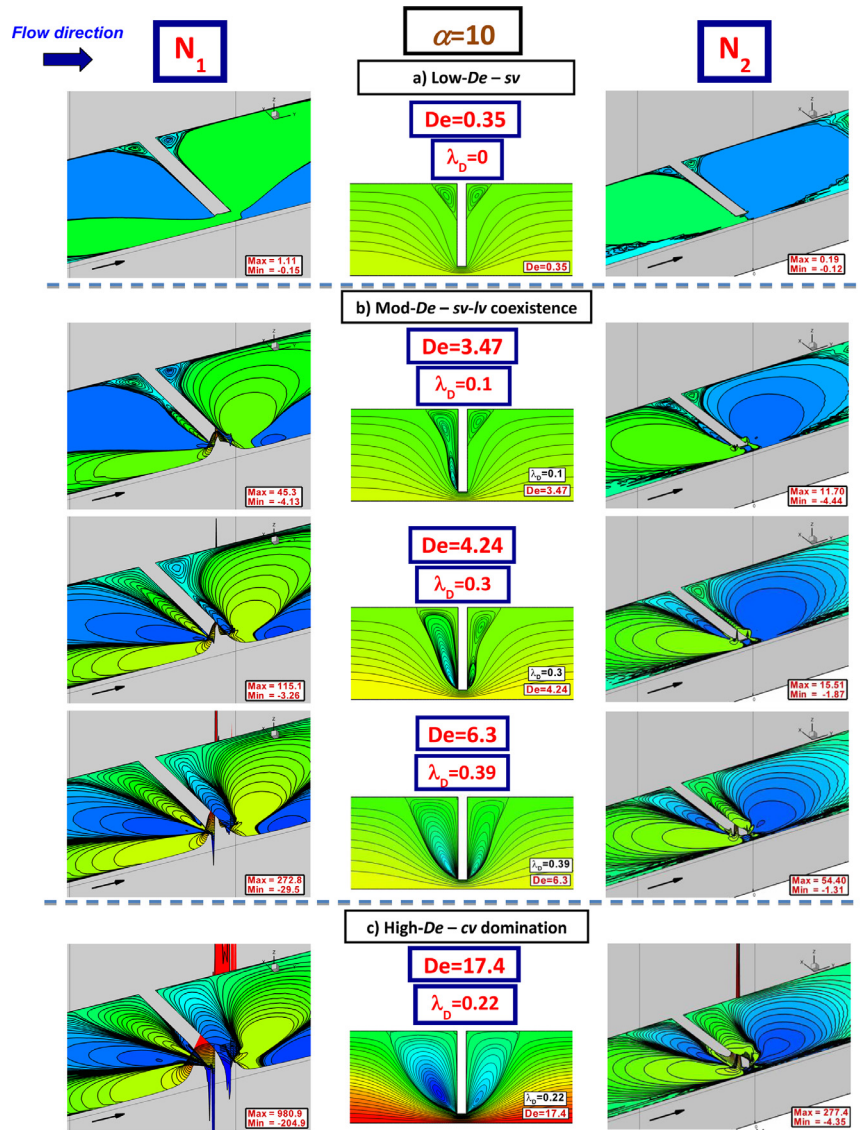


Fig. 13. Normal stresses v streamlines against De ; $\alpha = 10$.

phase, when both lip- and salient-corner vortices are present (Fig. 13b, moderate- De), three sample De -solutions are provided. At $De = 3.47$ and *upstream*, salient-corner and lip-centred stress patterns co-exist, whilst *downstream*, only isolated corner patterns are apparent. At the incremented larger level of $De = 4.24$, a single upstream pattern has formed upon merging of lip and corner forms, with locus centred nearby the re-entrant corner. Analogously at $De = 4.24$ and *downstream*, co-existent N_1 - N_2 structures are also visible, capturing the corresponding vortex structures as shown. Upon still further incrementation to $De = 6.3$, both stress-patterns and vortex-structures are depicted as coalesced, reflecting a strong single elastic-corner vortex; similar response is captured in both upstream and downstream zones. Covering the final phase of elastic corner-vortex domination, captured here at $De = 17.4$, large vortex-like stress-patterns emerge, both upstream and downstream. At this stage, the streamline loci have detached from the contraction front and back-faces. This position correlates with the emergence of sharp negative N_1 -peaks around the same wall-locations in the re-entrant corner vicinity (also appearing at $De = 6.3$; being less apparent in N_2 -plots).

Trends on vortex stress-maxima The associated trends in N_{1max} and N_{2max} are plotted against rate-rise in graphical form within

Fig. 14, corresponding to values at the centre of the vortex-like stress-patterns. Consistently, with Q -rise, the *salient-corner* N_{1max} and N_{2max} of Fig. 14a, reflect analogous trends to those observed in vortex-intensity (Fig. 6a). Downstream response is always delayed to that upstream, and N_{2max} represents a suppressed form of N_{1max} (but constituting more than 50% of N_{1max}). Beyond the station at which a lip-vortex appears, N_{1max} considerably strengthens, as noted both upstream and downstream; a feature present but less prominent in N_{2max} . Equivalently, on tracking the lip- to elastic corner-vortex and normal-stress activity of Fig. 14b, two phases of rising N_{1max} may be identified. The *first-phase* corresponds to that of lip-vortex formation, alongside its co-existence with the salient-corner structure (here, N_{1max} and N_{2max} coincide); the *second-phase* corresponds to that of domination from an elastic corner-vortex (transition indicated with a dashed-line). In N_{2max} -data, the onset of this second-phase is marked by an initial drop, that is then followed by a subsequent rise (ultimately, contributing $\sim 80\%$ to N_{1max}).

To help complete the picture, Fig. 15 compares and contrasts viscometric equivalent normal stress field patterns, in both shear (centre) and extension (right), against present complex flow solutions (left) through the same phases of Fig. 13. In sight of this

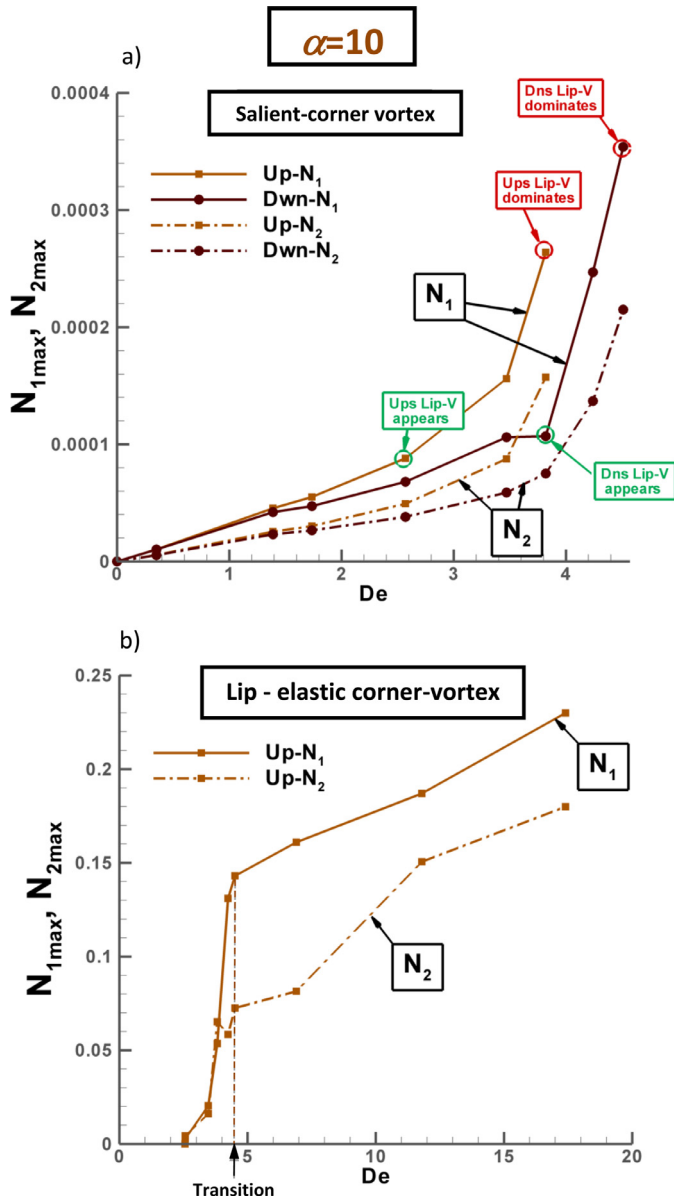


Fig. 14. Vortex-structure N_{1max} and N_{2max} against De ; a) sv, b) lv-cv; $\alpha = 10$.

evidence, one may infer that preferential rheology to govern N_1 is indeed a crucial factor in controlling vortex activity, and from a field distributional perspective, is largely dictated by normal stress response in shear. So, earlier suspicions, as expressed by Boger et al. [5] and Rothstein and McKinley [9], within a particular flow configuration and at a specific rate, may now be qualified; that is - 'whether it is extensional viscosity differences between fluids, or other influences such as their differences in normal-stress response in shear, that ultimately prove responsible for the particular vortex patterns that emerge'. Here, on the evidence supplied above, we favour the normal-stress response in shear as the overriding solution property, which consistently governs trends in flow patterns and distributions in stress/vortex activity within the vortex cells. Nevertheless normal-stress maxima, recorded through normal-stress-ratio, correlate well with the vortex-phasing observed experimentally. As such, one notes particularly the increased influence of extensional normal-stress contributions, that themselves dictate the dominance of an elastic corner-vortex over a salient-corner vortex (see Fig. 12).

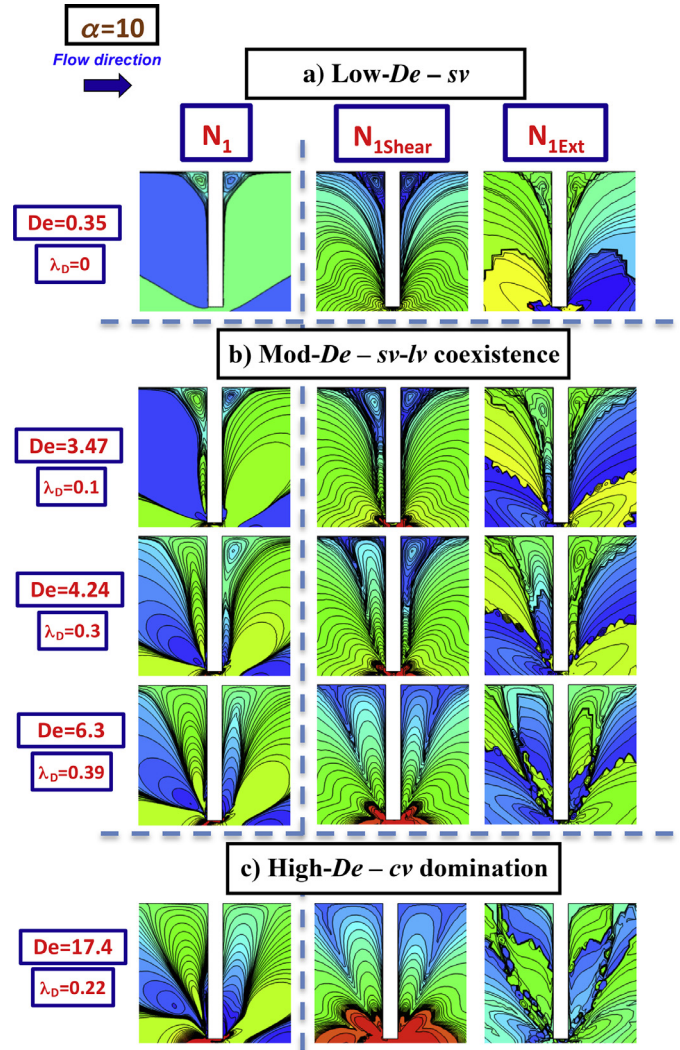


Fig. 15. Vortex-structure v viscometric N_{1Shear} and N_{1Ext} against De ; $\alpha = 10$.

6. Conclusions

In a recent study [10], experimental epd and vortex-dynamics data were reported for the flow a Boger PAA/CS-based Boger fluid, whilst changing contraction-ratio $\alpha = \{2, 4, 6, 8, 10\}$. Despite the qualitative agreement obtained, with a FENE-CR($\beta = 0.85, L$) model, the precise capture of the experimental- epd data for $\alpha=4$ remained somewhat lacking; gathering a maximum predicted- epd of only 30% at $De \sim 35$ - that is, against an experimental target value of 44% excess at much lower level of $De \sim 1.4$. There, $L = \{3, 6, 10\}$ and a fluid relaxation-time (λ_1)-increase protocol was used. In the present paper, we have presented a major modelling advance in closely-matching such experimental findings, whilst adopting the same flow configurations. This has only proved possible by appealing to the recently-proposed continuum-based swanINNFM model [24]; whilst employing parameters of ($\beta = 0.9; L = 5; \lambda_D$) and under a flow-rate (Q)-incremental protocol (to replicate equivalent procedures as used in the experiments).

Most notably here, precise matching of experimental- epd has been obtained for all contraction-expansion geometric aspect-ratios tested; and this under an averaged single relaxation time (λ_1) approximation. For $\alpha \geq 4$, three main regions of experimental epd -response have been captured with upper-lower windows of dissipative- λ_D -factor employing the swanINNFM(q) model. Under

close examination for each α and within such experimental zones, characteristic *epd*-subsets have been identified and correlated with averaged λ_D -values. These *epd*-subsets increase in number with α -rise, providing an ever richer response. This has permitted the capture of *epd*-maximum levels, as in the experiments, of $\sim\{300, 144, 350, 550, 600\}\%$ for $\alpha = \{2, 4, 6, 8, 10\}$. To our knowledge, such matching is unprecedented in *continuum mechanics* for Boger-fluids and circular contractions. An additional complication arose experimentally, in that larger Q -levels (larger deformation-rates) were required with α -rise, to capture the full history of *epd*-rise. Hence naturally, some λ_D -adjustment was found necessary to match the corresponding experimental observations. Here, a complex non-linear relationship has been constructed on λ_D against Q -rise, exposed through a piece-wise step-function in *epd*-subsets. This provides evidence for the necessity of a multimode representation in the dissipative $\phi(\lambda_D \dot{\epsilon})$ -functional.

In addition, a detailed description of the ensuing Q -rise flow-structure has been derived, related through counterpart vortex-dynamics. The outcome agrees tightly with the experimental findings of [10] across all contraction ratios, such that a change of flow regime is captured numerically with swanINNFM(q) $\lambda_D \neq 0$ solutions at the deformation-rates reported experimentally. These transitions are observed for $\alpha \geq 4$, through *epd*-rise; and through kinematics, for $\alpha \geq 6$, with corner/lip-vortex coexistence, and subsequent elastic corner-vortex domination. With Q -rise and for $\alpha \geq 6$ ($\alpha = 10$ being the most representative - largest extension-rates), the complex vortex activity reflects three distinct phases. *Firstly*, at low Q -levels, Newtonian-like salient-corner vortex-enhancement is apparent, with concave separation-lines; *secondly*, this phase is then supplanted by lip-vortex formation and co-existence of lip-with-salient-corner vortices at intermediate deformation-rates; and *finally*, lip-vortex domination and prevalence towards a convex elastic corner-vortex. In contrast, for $\alpha \leq 4$, only salient-corner vortex enhancement is predicted, as in [10]. Moreover, these vortex-growth patterns agree with previous experimental findings for PIB/PB Boger fluids and flow through circular contractions [5], where salient-corner and lip-vortices were found to co-exist. Within the context of contraction-expansion flow and PAA/CS Boger fluids, our predictions also reproduce the trends found experimentally in [9], on lip-vortex to elastic corner-vortex formation. Consistently $\alpha \geq 6$ -solutions, with more balanced shear-extension normal-stress-ratios (greater extensional stress influence), reveal flow domination governed by an elastic corner-vortex; whilst $\alpha = 4$ -solutions, with larger normal-stress-ratios, provide exclusively salient-corner vortex-activity. The $\alpha = 2$ solutions remain an isolated case, with its experimentally large maxima in *epd* of ~ 3 , within a notably low and narrow Q -range (low extension-rates generated). This position is reflected in *epd*, on a single λ_D -prediction-window of outstandingly large λ_D -bounds [$\sim O(10^2)$ upper]; and through its kinematics, producing a single phase of symmetric salient-corner vortex-enhancement.

Covering both upstream and downstream vortex activity, it is increased elastic effects that are identified as the origin of salient-to-lip vortex location and intensity, governing their presence, co-existence, coalescence and evolution. This has been recognised through flow response, in patterns of first and second normal stress differences, $N_1 - N_2$, and trends in $N_{1max} - N_{2max}$ and first normal stress ratio. Vortex structures that reflect existence, location and evolution, directly correlate with vortex-like patterns in $N_1 - N_2$ fields. Consistently, the transition from the lip-vortex phase to the elastic corner-vortex phase is reflected in $N_{1max} - N_{2max}$, and N_1 -trends in particular. Hence, one may infer that N_1 preferential rheology is a crucial factor in controlling vortex activity, largely dictated by response from normal stress in shear. Here, shearing normal-stress contributions are held chiefly responsible for the internal patterns supported within the vortex-cells (*salient*; *salient-*

to-lip; *lip-to-elastic*); whilst relative strength of extensional to shear normal stresses, is correlated with elected vortex-phasing, between salient-corner vortex and elastic corner-vortex structures. As such, this work helps clarify earlier statements made on the subject, see Boger et al. [5], Rothstein and McKinley [9].

Acknowledgement

Financial support (scholarship to J.E.L.-A.) from Consejo Nacional de Ciencia y Tecnología (CONACYT, México) is gratefully acknowledged.

Appendix A. Scaling factor between experimental and numerical data

In the experimental work of Pérez-Camacho et al. [10], the Deborah number De is defined as follows:

$$De = \lambda_{1\text{exp}} \frac{4Q}{\pi R_c^3}, \quad (\text{A.1})$$

whilst for numerical simulations, a measure of fluid viscoelasticity is given by a Deborah group number De^{sim} of the form:

$$De^{\text{sim}} = \lambda_{1\text{sim}} \frac{Q}{\pi R_c^3} = \lambda_{1\text{sim}} \frac{\bar{U}}{L}. \quad (\text{A.2})$$

Note that $\lambda_{1\text{sim}}$ is held at a unity level, and change in elasticity is driven by Q -increase, mimicking closely experimental protocols. Hence, equating experimental and computational characteristic deformation-rates, one obtains:

$$\frac{De}{4\lambda_{1\text{exp}}} = \frac{De^{\text{sim}}}{\lambda_{1\text{sim}}}, \quad (\text{A.3})$$

and on introducing relevant physical quantities ($\lambda_{1\text{exp}} = 0.174\text{s}$, as provided experimentally), one finally extracts:

$$De = \frac{1}{1.44} De^{\text{sim}}. \quad (\text{A.4})$$

References

- [1] K. Walters, M.F. Webster, The distinctive CFD challenges of computational rheology, *Int. J. Numer. Methods Fluids* 43 (2003) 577–596.
- [2] R.G. Owens, T.N. Phillips, *Computational Rheology*, Imperial College Press, London, 2002.
- [3] D.V. Boger, K. Walters, *Rheological Phenomena in Focus*, Elsevier Science Publishers B.V., 1993.
- [4] M.F. Webster, H.R. Tamaddon-Jahromi, F. Belblidia, *Computational Rheology*, in: C. Gallegos (Ed.), *Encyclopedia of Life Support Systems Rheology (EOLSS-UNESCO)*, vol. 1, 2010, p. 205.
- [5] D.V. Boger, D.U. Hur, R.J. Binnington, Further observations of elastic effects in tubular entry flows, *J. Non-Newton. Fluid Mech.* 20 (1986) 31–49.
- [6] D.V. Boger, R.J. Binnington, Circular entry flows and fluid M1, *J. Non-Newton. Fluid Mech.* 35 (1990) 339–360.
- [7] G.H. McKinley, W.P. Raiford, R.A. Brown, R.C. Armstrong, Nonlinear dynamics of viscoelastic flow in axisymmetric abrupt contractions, *J. Fluid Mech.* 223 (1991) 411–456.
- [8] J.P. Rothstein, G.H. McKinley, Extensional flow of a polystyrene Boger fluid through a 4:1:4 axisymmetric contraction/expansion, *J. Non-Newton. Fluid Mech.* 86 (1999) 61–88.
- [9] J.P. Rothstein, G.H. McKinley, The axisymmetric contraction-expansion: the role of extensional rheology on vortex growth dynamics and the enhanced pressure drop, *J. Non-Newton. Fluid Mech.* 98 (2001) 33–63.
- [10] M. Pérez-Camacho, J.E. López-Aguilar, F. Calderas, O. Manero, M.F. Webster, Pressure-drop and kinematics of viscoelastic flow through an axisymmetric contraction-expansion geometry with various contraction-ratios, *J. Non-Newton. Fluid Mech.* 222 (2015) 260–271.
- [11] M. Aoubacar, H. Matallah, H.R. Tamaddon-Jahromi, M.F. Webster, Numerical prediction of extensional flows in contraction geometries: hybrid finite volume/element method, *J. Non-Newton. Fluid Mech.* 104 (2002) 125–164.
- [12] M.A. Alves, P.J. Oliveira, F.T. Pinho, Benchmark solutions for the flow of Oldroyd-B and PTT fluids in planar contractions, *J. Non-Newton. Fluid Mech.* 110 (2003) 45–75.
- [13] D.M. Binding, P.M. Phillips, T.N. Phillips, Contraction/expansion flows: the pressure drop and related issues, *J. Non-Newton. Fluid Mech.* 137 (2006) 31–38.

- [14] J.P. Aguayo, H.R. Tamaddon-Jahromi, M.F. Webster, Excess pressure-drop estimation in contraction and expansion flows for constant shear-viscosity, extension strain-hardening fluids, *J. Non-Newton. Fluid Mech.* 153 (2008) 157–176.
- [15] K. Walters, M.F. Webster, H.R. Tamaddon-Jahromi, Experimental and computational aspects of some contraction flows of highly elastic liquids and their impact on the relevance of the Couette correction in extensional rheology, in: *Proc. 2nd Southern African Conference on Rheology (SASOR 2)*, 2008, pp. 1–6.
- [16] K. Walters, M.F. Webster, H.R. Tamaddon-Jahromi, The numerical simulation of some contraction flows of highly elastic liquids and their impact on the relevance of the Couette correction in extensional rheology, *Chem. Eng. Sci.* 64 (2009) 4632–4639.
- [17] H.R. Tamaddon-Jahromi, M.F. Webster, P.R. Williams, Excess pressure drop and drag calculations for strain-hardening fluids with mild shear-thinning: Contraction and falling sphere problems, *J. Non-Newton. Fluid Mech.* 166 (2011) 39–950, doi:10.1016/j.jnnfm.2011.04.009.
- [18] P. Szabo, J.M. Rallison, E.J. Hinch, Start-up of flow of a FENE-fluid through a 4:1:4 constriction in a tube, *J. Non-Newton. Fluid Mech.* 72 (1997) 73–86.
- [19] J. Castillo-Tejas, O. Castejón-González, J.F.J. Alvarado, O. Manero, Prediction of excess pressure drop in contraction–expansion flow by molecular dynamics: Axisymmetric and planar configurations, *J. Non-Newton. Fluid Mech.* 210 (2014) 1–11.
- [20] M. Aoubacar, M.F. Webster, A cell-vertex finite volume/element method on triangles for abrupt contraction viscoelastic flows, *J. Non-Newton. Fluid Mech.* 98 (2001) 83–106.
- [21] M. Aoubacar, H. Matallah, M.F. Webster, Highly elastic solutions for Oldroyd-B and Phan-Thien/Tanner fluids with a finite volume/element method: planar contraction flows, *J. Non-Newton. Fluid Mech.* 103 (2002) 65–103.
- [22] R.I. Tanner, *Engineering Rheology*, Second ed., Oxford University Press, Oxford, 2000.
- [23] M.S.N. Oliveira, P.J. Oliveira, F.T. Pinho, M.A. Alves, Effect of contraction ratio upon viscoelastic flow in contractions: the axisymmetric case, *J. Non-Newton. Fluid Mech.* 147 (2007) 92–108.
- [24] H.R. Tamaddon-Jahromi, I.E. Garduño, J.E. López-Aguilar, M.F. Webster, Predicting large experimental excess pressure drops for Boger fluids in contraction–expansion flow, *J. Non-Newton. Fluid Mech.* 230 (2016) 43–67, doi:10.1016/j.jnnfm.2016.01.019.
- [25] J.E. López-Aguilar, H.R. Tamaddon-Jahromi, M.F. Webster, K. Walters, Numerical vs experimental pressure drops for Boger fluids in sharp-corner contraction flow, *Phys. Fluids* 28 (2016) *In press*.
- [26] S. Nigen, K. Walters, Viscoelastic contraction flows: comparison of axisymmetric and planar configurations, *J. Non-Newton. Fluid Mech.* 102 (2002) 343–359.
- [27] J.L. White, A.B. Metzner, Development of constitutive equations for polymeric melts and solutions, *J. Appl. Polym. Sci.* 7 (1963) 1867–1889.
- [28] M.D. Chilcott, J.M. Rallison, Creeping flow of dilute polymer solutions past cylinders and spheres, *J. Non-Newton. Fluid Mech.* 29 (1988) 381–432.
- [29] B. Debbaut, M.J. Crochet, Extensional effects in complex flows, *J. Non-Newton. Fluid Mech.* 30 (1988) 169–184.
- [30] B. Debbaut, M.J. Crochet, H. Barnes, K. Walters, Extensional effects in inelastic liquids, in: *Xth International Congress on Rheology*, Sydney, 1988, pp. 291–293.
- [31] M. Nyström, H.R. Tamaddon Jahromi, M. Stading, M.F. Webster, Extracting extensional properties through excess pressure drop estimation in axisymmetric contraction and expansion flows for constant shear-viscosity, extension strain-hardening fluids, *Rheol. Acta* 55 (2016) 373–396.
- [32] F. Belblidia, I.J. Keshtiban, M.F. Webster, Stabilised computations for viscoelastic flows under compressible implementations, *J. Non-Newton. Fluid Mech.* 134 (2006) 56–76.
- [33] F. Belblidia, I.J. Keshtiban, M.F. Webster, Alternative subcell discretisations for viscoelastic flow: stress interpolation, *J. Non-Newton. Fluid Mech.* 146 (2007) 59–78.
- [34] F. Belblidia, H. Matallah, M.F. Webster, Alternative subcell discretisations for viscoelastic flow: velocity-gradient approximation, *J. Non-Newton. Fluid Mech.* 151 (2008) 69–88.
- [35] J.E. López-Aguilar, M.F. Webster, H.R. Tamaddon-Jahromi, O. Manero, High-Weissenberg predictions for micellar fluids in contraction–expansion flows, *J. Non-Newton. Fluid Mech.* 222 (2015) 190–208.
- [36] J.E. López-Aguilar, M.F. Webster, H.R. Tamaddon-Jahromi, O. Manero, Convoluted models and high-Weissenberg predictions for micellar thixotropic fluids in contraction–expansion flows, *J. Non-Newton. Fluid Mech.* 232 (2016) 55–66.